



Designed oxygen carriers from macroporous LaFeO₃ supported CeO₂ for chemical-looping reforming of methane



Yane Zheng^{a,b}, Kongzhai Li^{a,b,*}, Hua Wang^{a,b}, Dong Tian^{a,b}, Yuhao Wang^{a,b}, Xing Zhu^{a,b}, Yonggang Wei^{a,b}, Min Zheng^{a,b}, Yongming Luo^c

^a State Key Laboratory of Complex Nonferrous Metal Resources Clean Utilization, Kunming University of Science and Technology, Kunming 650093, China

^b Faculty of Metallurgical and Energy Engineering, Kunming University of Science and Technology, Kunming 650093, China

^c Faculty of Environmental Engineering, Kunming University of Science and Technology, Kunming 650093, China

ARTICLE INFO

Article history:

Received 18 April 2016

Received in revised form 9 August 2016

Accepted 11 August 2016

Available online 24 August 2016

Keywords:

Chemical-looping reforming of methane

Syngas and hydrogen

CeO₂/LaFeO₃

Interface

Carbon deposition

ABSTRACT

Chemical-looping reforming of methane (CLRM) offers an effective approach for coproducing syngas and pure hydrogen. In this work, CeO₂ nano particles (2–3 nm) are well dispersed on the wall surface of three-dimensional ordered macroporous (3DOM) LaFeO₃, obtaining a highly efficient oxygen carrier for the CLRM technology. The physical and chemical properties of the oxygen carriers were characterized by SEM, TEM, H₂-TPR, XPS, XRD, CH₄-TPR and CH₄-TPD techniques. It is found that the presence of CeO₂ on LaFeO₃ results in the formation of Ce³⁺ and Fe²⁺ due to the CeO₂-LaFeO₃ interaction. The coexistence of Ce³⁺ and Fe²⁺ ions induces abundant oxygen vacancies on the mixed oxides, which strongly improves the reducibility, oxygen mobility and reactivity for methane oxidation. The presence of CeO₂ also improves the resistance towards carbon deposition formation, and this allows the CeO₂/LaFeO₃ materials own high available oxygen storage capacity (available OSC, the maximum amount of oxygen consumed by methane reduction without the formation of carbon deposition). It is also noted that the agglomeration of CeO₂ nano particles would reduce the reactivity of oxygen carriers. Among all the obtained samples, the 10% CeO₂/LaFeO₃ sample exhibits the highest yields of syngas (9.94 mmol g⁻¹) and pure hydrogen (3.38 mmol g⁻¹) without the formation of carbon deposition, which are much higher than that over the pure LaFeO₃ sample (5.73 mmol g⁻¹ for syngas yield and 2.00 mmol g⁻¹ for hydrogen yield). In addition, the CeO₂/LaFeO₃ oxygen carrier also showed high stability during the successive CLRM testing either in the activity (yields of syngas and pure hydrogen) or structure (macroporous frameworks) aspect.

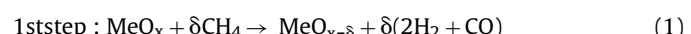
© 2016 Elsevier B.V. All rights reserved.

1. Introduction

Hydrogen is one of the most important base materials in the chemical industry, such as the production of methanol and ammonia, Fischer-Tropsch synthesis and petroleum refining processes. Hydrogen is also considered to be a clean energy source and carrier, which can be used in fuel cells [1,2]. Currently, the largest and most economical method of hydrogen production involves methane reforming with steam (CH₄ + H₂O → CO + 3H₂) [3,4]. This process produces syngas (a mixture of H₂ and CO) with a H₂/CO ratio of 3.0, which is undesirable in the subsequent chemical utilizations

(e.g., methanol production and Fischer-Tropsch synthesis where the syngas source with a H₂/CO ratio of 2.0 is expected). A water-gas shift reaction (CO + H₂O → CO₂ + H₂) is needed for obtaining pure hydrogen, resulting in additional energy consumption.

Chemical-looping reforming of methane (CLRM) technology provides a novel route to directly produce syngas with a H₂/CO ratio of 2.0 and pure hydrogen. This process mainly includes two reactions via using a metal oxide (MeO_x) as oxygen carrier, which can be described as follows [5,6]:



Syngas with a H₂/CO ratio of 2.0 is obtained by the reaction of oxygen carrier with methane (the first step), and then the reduced oxygen carrier (MeO_{x-δ}) is re-oxidized to generate pure hydrogen by a water splitting reaction (the second step). The development of suitable oxygen carriers is a key challenge for optimizing the

* Corresponding author at: State Key Laboratory of Complex Nonferrous Metal Resources Clean Utilization, Kunming University of Science and Technology, Kunming 650093, China.

E-mail addresses: kongzhai.li@aliyun.com, kongzhai.li@foxmail.com, 776560951@qq.com (K. Li).

chemical-looping process. The oxygen carrier must possess high oxygen storage capacity (OSC), sufficient oxygen transport ability, high reactivity under alternating reducing and oxidizing conditions, good thermal stability and superior mechanical property for successive cycles at high temperatures and in the presence of H₂O [7].

La-based perovskite-type oxides with a general formula of LaBO₃ are known to contain large concentrations of vacancies in their structure, reversibly pick up and deliver oxygen at high temperatures and exhibit mixed-type conductivity for the necessary transfer of anions, vacancies and electrons [8]. Dai et al. [9,10] reported that LaFeO₃ is an attractive oxygen carrier for the partial oxidation of methane to CO and H₂ due to the abundant vacancies on the surface and high mobility of lattice oxygen in the bulk. Mihai et al. [11] discussed the determination factors for controlling the selectivity of syngas produced by methane partial oxidation using chemical looping on LaFeO₃ perovskite oxygen carriers. Nearly pure syngas was generated via controlling the oxidation degree of the reduced oxygen carriers in the re-oxidation step. La_xSr_{1-x}FeO_{3-δ} perovskite was also found to be well suited for chemical-looping reforming applications [12,13]. The result from Sarshar et al. [14] reported that the LaMn0.7Fe0.3O_{3.15@mSiO2} core-shell materials showed superior reactivity in methane oxidation and high stability during repeated chemical looping process. They attribute the high stability to the protective role against sintering of the mesoporous silica shells surrounding the perovskite core particles. Li et al. [15–17] prepared a series of Fe₂O₃@La_{1-x}Sr_xFeO_{3-δ} core-shell oxygen carriers, which maintained satisfactory CLRM performance within a temperature range of 800–900 °C. The stability of the perovskite-based oxygen carrier is confirmed by a 50 cycle continuous redox experiment. Coke formation was also found to be minimal.

CeO₂ is one of the most attractive oxygen storage materials that have a high OSC due to its ability to release/acquire oxygen through redox processes involving the Ce⁴⁺/Ce³⁺ couple [18]. Ce-based materials have been studied as oxygen carriers for the CLRM process. CeO₂ showed high selectivity for the conversion of methane to syngas by a chemical looping process [19]. The incorporation of ZrO₂ into CeO₂ lattice could enhance the formation rates of H₂ and CO, but it will reduce the selectivity of syngas. Our previous study showed that the appropriate calcination temperature could enhance the reactivity of CeO₂-ZrO₂ solid solution for CLRM [20]. We also investigated a series of CeO₂-Fe₂O₃ complex oxides for CLRM [21,22]. The results showed that an appropriate Fe₂O₃ content could improve the reactivity and redox properties of CeO₂ for selective oxidation of methane to syngas with a H₂/CO ratio of 2.0. Ce_{0.8}Gd_{0.2}O_{2-δ} also gave outstanding oxygen permeation and high reactivity for methane oxidation [23]. The thermodynamic analysis indicated that ceria based oxides showed a low Gibbs free energy changes for the reactions with water and methane [24]. CeO₂ also shows good performance on supports as a redox oxygen carrier. Jeong et al. [25] used ZrO₂-supported CeO₂ as an oxygen carrier for the CLRM process. The results revealed that the high-temperature stable ZrO₂ support allowed for good dispersion of the CeO₂ particles, which suppressed the sintering of CeO₂ during repeated cyclic operations. Miller et al. [26] reported that the incorporation of CeO₂ to the natural ore hematite strongly modified the reduction behavior in comparison to that of CeO₂ and hematite alone. The addition of even 5 wt% CeO₂ could enhance the reaction capacity of the Fe₂O₃ oxygen carrier by promoting the decomposition and partial oxidation of methane. Our previous work also showed that the presence of CeO₂ on Fe₂O₃ oxides significantly improved the redox performance of oxygen carriers and increased the hydrogen yield because of the chemical interaction between Ce and Fe species [27]. Ceria also possesses good electronic and ionic conductivity, which can

decrease carbon deposition during methane reforming when it is used as a support or an additive [28,29].

Combination of CeO₂ and perovskite type oxides also attracted considerable interest due to the potential synergistic effect. Alifanti et al. [30] investigated the catalytic activity of LaCoO₃/Ce_{1-x}Zr_xO₂ catalysts for toluene combustion. High performance was demonstrated for this composite oxide due to the increased specific surface area and relatively high oxygen mobility. Since no new phases were detected, the observed synergistic effect can only be attributed to the interaction between LaCoO₃ and Ce_{1-x}Zr_xO₂ particles at the interfaces. Similar phenomena were also observed in the LaMnO₃/CeO₂ system [31]. The coupling of Mn⁴⁺/Mn³⁺ and Ce⁴⁺/Ce³⁺ couples strongly enhanced the redox capacity of the surface species, resulting in high catalytic activity at low temperatures. As a mixed-conducting oxide, the CeO₂-LaFeO₃ material showed superior electrical conductivity and high activity for direct oxidation of hydrocarbon in solid oxide fuel cells [32]. This material also showed high stability in long-term testing although the element Fe and some unknown phases separated from the bulk material of LaFeO₃ in the reducing atmosphere at high temperature [33]. This suggests the occurrence of the interaction between CeO₂ and LaFeO₃ in a deep level.

Three-dimensionally ordered macroporous (3DOM) materials are more suitable for gas-solid reactions due to the uniform pore sizes (>50 nm) and well-defined periodic structures. The uniform structure owing large external surface areas allows low mass-transfer resistances and provides more reaction active sites. Zhang et al. [34,35] suggested that 3DOM CeO₂-based catalysts showed higher catalytic activities for soot combustion than corresponding disordered macroporous ones, which benefits from the enhanced contact efficiency between soot and ordered macroporous structure. On the other hand, 3DOM CeO₂-based oxides showed significantly faster kinetics and higher thermal stability during water splitting reaction compared with nonporous samples [36]. 3DOM materials also display considerable potential as catalyst support. Wei et al. [37,38] suggested that noble metals well dispersed on the inner wall of both 3DOM LaFeO₃ and Ce_{1-x}Zr_xO₂ oxides exhibited high activity and stability for catalytic soot oxidation. Liu et al. [39] also reported that in comparison with nonporous Au/CeO₂-Co₃O₄ catalyst, 3DOM Au/CeO₂-Co₃O₄ catalysts showed superior catalytic activity, selectivity, and stability for CO preferential oxidation in H₂-rich gases. Noble metals supported on 3DOM Co₃O₄ and La_{0.6}Sr_{0.4}MnO₃ exhibited lower apparent activation energy, better low-temperature reducibility and higher catalytic activity for toluene oxidation, which can be attributed to the stronger noble metal-3DOM oxides interaction [40,41]. Zhao et al. [42] reported that the 3DOM LaFeO₃ oxygen carrier exhibited much higher activity, repeatability, and stability as well as better resistance to carbon formation for the partial oxidation of methane compared to nonporous LaFeO₃.

All the above discussions suggest that combining CeO₂ with LaFeO₃ involving 3DOM structure may create a promising oxygen storage material for CLRM technology. Herein, we successfully prepared a series of 3DOM LaFeO₃-supported CeO₂ samples with well dispersed CeO₂ nanoparticles using a gas-bubble-assisted method. These 3DOM xCeO₂/LaFeO₃ materials are expected to own higher activity than the conventional LaFeO₃-based and CeO₂-based oxygen carriers for syngas and hydrogen generation via a CLRM process. We mainly focus on discussing the synergistic effect between CeO₂ and LaFeO₃ in oxidation and reduction conditions to gain insights into the CeO₂-LaFeO₃ interaction. Based on the discussions, the reaction mechanism including the reaction pathways of CH₄ oxidation and H₂O conversion for CLRM over 3DOM xCeO₂/LaFeO₃ is proposed at the first time.

2. Experimental

2.1. Oxygen carrier preparation

2.1.1. Synthesis of monodispersed poly methyl methacrylate (PMMA) microsphere and assembly template

The monodispersed, well-arrayed PMMA microspheres with an average diameter of ca. 200 nm were synthesized using a modified emulsifier-free emulsion polymerization technique according to previous procedures described [39,40].

2.1.2. Preparation of 3DOM LaFeO₃ supports

The preparation of 3DOM LaFeO₃ perovskite-type complex oxides was carried out by a hard-template method. The chemicals La(NO₃)₃·6H₂O (99.9%), Fe(NO₃)₃·9H₂O (99.9%), Ce(NO₃)₃·6H₂O (99.9%), ethylene glycol (EG, 99.9%), methanol (MeOH, 99.9%) were all purchased from Aladdin Reagent Company. The precursor solutions were obtained by mixing stoichiometric amounts of La(NO₃)₃·6H₂O and Fe(NO₃)₃·9H₂O into EG-MeOH solution (EG/MeOH volumetric ratio=2:1) at room temperature (RT). 10 mmol mixed metal nitrates were dissolved with 10 mL of EG-MeOH solution by stirring in a 100 mL beaker at RT for 2 h to obtain a transparent solution. Then 10 g of the PMMA template was soaked in the above mixed solution for 4 h, so that the voids of the template microspheres were completely filled with the transparent solution. After being filtered, the obtained wet powders were dried at 60 °C for 24 h. Thereafter, the samples were further aged at 600 °C for 2 h to obtain the final 3DOM LaFeO₃.

2.1.3. Preparation of 3DOM xCeO₂/LaFeO₃ oxygen carriers

The 3DOM xCeO₂/LaFeO₃ samples were prepared via a gas-bubble-assisted method. A desired amount of Ce(NO₃)₃·6H₂O was added into the deionized water at RT under vigorous stirring for 1 h to obtain a transparent solution. A desired amount (theoretical CeO₂ loading = 5.0, 10.0 or 20.0 wt%) of the LaFeO₃ support was then added to the Ce(NO₃)₃ solution, and the obtained suspension was subjected to stirring and bubbling with N₂ (100 mL/min) for 6 h. The solid was collected by filtration, followed by washing with deionized water and ethanol and drying at 60 °C for 12 h. The dried samples were calcined at 450 °C for 2 h with a ramp rate of 2 °C/min, obtaining the 3DOM xCeO₂/LaFeO₃ oxygen carriers. The obtained samples were labelled as 5%CeO₂/LaFeO₃, 10%CeO₂/LaFeO₃ and 20%CeO₂/LaFeO₃, respectively.

2.2. Physical and chemical characterization

The morphology of the oxygen carrier was observed by scanning electron microscopy (SEM) on a NOVA NANOSEM 450 instrument using an accelerating voltage of 3 kV. The SEM samples were dusted on an adhesive conductive carbon belt attached to a copper disk.

For transmission electron microscopy (TEM), a JEOL JEM-2100 microscope was used with a LaB6 filament operating at 200 kV. The specimens were crushed into a powder and immersed in a small volume of ethanol. After sonicating the mixture for 10 min, a droplet of the suspension was allowed to dry on a holey carbon/Formvar-coated copper TEM grid.

H₂ temperature-programmed reduction (H₂-TPR) profiles were obtained from RT to 900 °C. Experimental data was collected using a TPR Win instrument, version 1.50 software (produced by Quantachrome Instruments Co.). 100 mg of catalyst was used along with a heating rate of 10 °C/min. After a standard cleaning pre-treatment, the TPR was carried out in a flow of 10% H₂/Ar (25 mL/min) up to 900 °C.

The X-ray photoelectron spectroscopy (XPS) experiments were carried out by a PHI 5000 Versaprobe II system equipped with a monochromatic Al-Ka X-ray source. The spectra were registered

after purging the samples at ambient temperature under vacuum (residual pressure <10⁻⁷ Pa). An electron flood gun compensated the sample charging during the measurement. The electron take off angle was 45° with respect to the sample surface, and the analyser was operated in constant pass energy mode (46.95 eV). The C 1 s signal at 284.8 eV was used as an internal standard for calibration of the XPS-signals.

CH₄-TPR over the oxygen carriers (ca. 100 mg) was conducted using a microreactor system (CATLAB, produced by Hiden Analytical Co., England). Prior to each experiment, the sample was pre-treated in flowing pure Ar (99.99%, 50 mL/min) at 400 °C for 1 h and cooled to RT followed by purging with Ar for 30 min. Thereafter, the pre-treated sample was exposed to 5% CH₄/Ar (50 mL/min) at RT for 30 min, and then, the temperature was increased at a rate of 10 °C/min to 900 °C. The gas was analysed using an online mass spectrometer (QGA, produced by Hiden Analytical Co., England).

The CH₄/O₂ pulse reactions were also performed using the microreactor system. Prior to the measurements, 10 mg of the sample was purged in flowing pure Ar (99.99%, 50 mL/min) gas at RT for 30 min followed by increasing the temperature at a rate of 10 °C/min to 800 °C. Subsequently, pulses of 10% CH₄/Ar were sequentially admitted to the reactor. A pulse of CH₄ gas was introduced for 60 s using a six-way gas-sampling valve equipped with a measuring ring (100 μL). After 25 sequences of CH₄/Ar pulses, the sample was purged with pure Ar for 30 min. Then, pulses of 25% O₂/Ar were employed. This oxidation period was divided into 25 pulses (complete oxidation) and 15 pulses (incomplete oxidation), respectively. The gas was analysed using an online mass spectrometer.

CH₄-TPD over the oxygen carriers (ca. 100 mg) was also conducted using the microreactor system. Prior to each experiment, the sample was pre-treated in flowing pure Ar (50 mL/min) at 400 °C for 1 h and cooled to RT followed by purging with pure Ar for 30 min. Thereafter, the pre-treated sample was exposed to 5% CH₄/Ar (50 mL/min) at RT for 30 min, and then, the gas was switched to Ar (50 mL/min) for 30 min. After that, the temperature was increased at a rate of 10 °C/min to 900 °C in flowing Ar (50 mL/min).

The crystal phases of the oxygen carriers were measured by a powder X-ray diffractometer (Rigaku) using Cu Kα radiation ($\lambda = 0.15406 \text{ nm}$). The X-ray tube was operated at 40 kV and 15 mA. The XRD patterns were carried out for 2θ values from 10° to 90° with a scanning rate of 5°/min.

2.3. Reactivity tests

2.3.1. Methane reduction step

The reactions of the oxygen carriers with methane were carried out in a tubular fixed-bed reactor at atmospheric pressure. Oxygen carriers (0.3 g) with a particle size of 20–40 mesh were loaded into the quartz reactor. Prior to each measurement, pure N₂ (99.99%, 100 mL/min,) was flowed to the reactor for 30 min at 300 °C to remove the possible impurities on the oxygen carriers. The CH₄ isothermal reaction was conducted using CH₄ flowing over the oxygen carriers at 800 °C for 5 min. The gas flow rate of methane mixed gas 5% CH₄/Ar was controlled at 200 mL/min. The gas components were analyzed by a gas analyzer (GASBOARD-3100, Wuhan cubic optoelectronic Co., Ltd.) and a gas chromatograph (Agilent 7890A GC System, produced by Agilent Co.).

2.4. Water oxidation step

After the reaction between methane and the oxygen carriers, pure N₂ (99.99%, 100 mL/min) was flowed into the reactor for 30 min. Then, the steam carried by N₂ gas (99.99%, 200 mL/min) was introduced into the reactor for 20 min. The steam was gener-

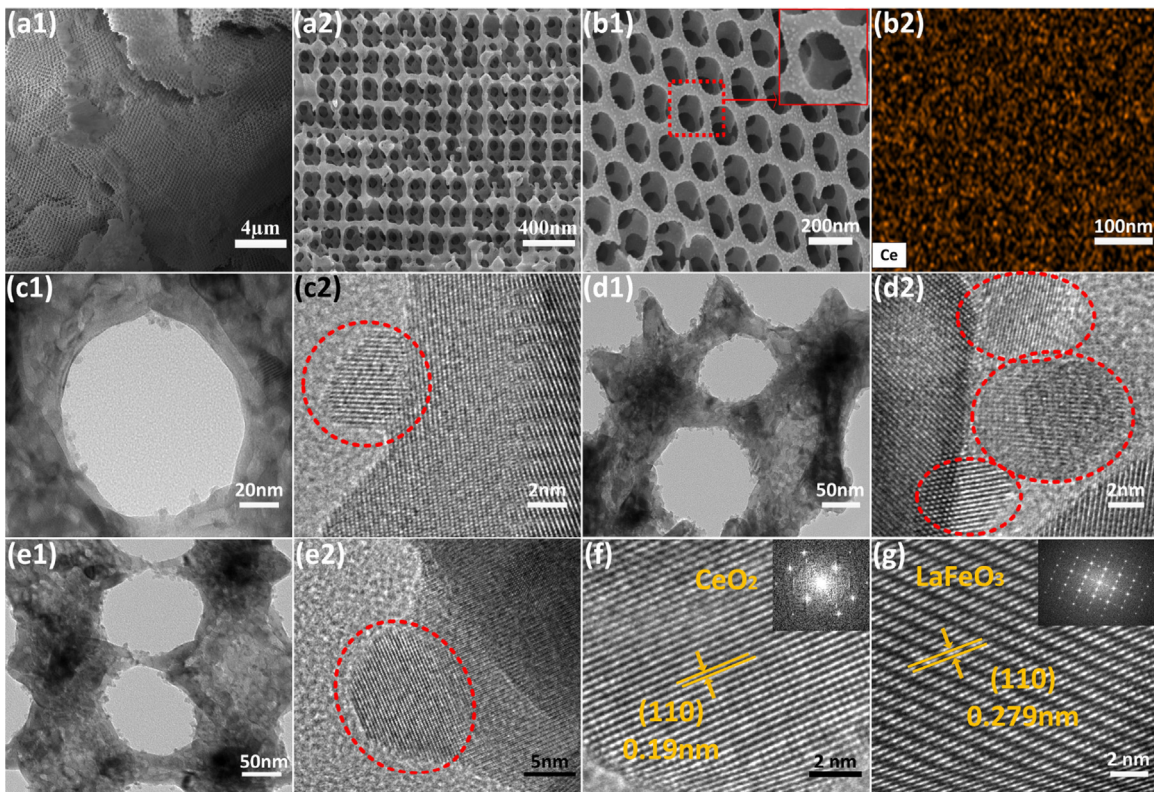


Fig. 1. Morphological and macrostructural characterizations of the 3DOM LaFeO₃ and xCeO₂/LaFeO₃. (a1, a2) SEM images of 3DOM LaFeO₃; (b1) SEM images of 10%CeO₂/LaFeO₃; (b2) Ce EDS map for 10% CeO₂/LaFeO₃; (c1, c2) TEM images of 5%CeO₂/LaFeO₃; (d1, d2) TEM images of 20%CeO₂/LaFeO₃; (e1, e2) TEM images of 10%CeO₂/LaFeO₃; (f) HRTEM image of the CeO₂ particle in the 10%CeO₂/LaFeO₃ and the corresponding Fourier transform image (inset); (g) HRTEM image of the LaFeO₃ in the 10%CeO₂/LaFeO₃ and the corresponding Fourier transform image (inset).

ated by heating water at 60 °C, and the N₂ carrier gas was bubbled to carry the steam into the reactor. The reaction temperature in the entire process was maintained at 800 °C. The gas components were analysed using a gas analyser (GASBOARD-3100, Wuhan cubic optoelectronic Co., Ltd.). All of the gases were purchased from the Messer Company.

The CO selectivity was calculated as follows:

$$\text{CO selectivity} = \frac{\text{moles of CO produced}}{\text{moles of methane consumed}} \times 100\% \quad (1)$$

3. Results

The morphology and macrostructures of 3DOM LaFeO₃ and xCeO₂/LaFeO₃ were investigated using SEM and TEM technologies, as shown in Fig. 1. The macroporous LaFeO₃ possesses open and periodic three-dimensional (3D) frameworks with an average diameter of 100 ± 10 nm. The results in Fig. 1b1 indicate that the 10%CeO₂/LaFeO₃ sample also possesses a well-defined 3DOM structure with a macropore diameter of ca. 100 ± 10 nm. This phenomenon indicates that the loading of CeO₂ did not induce significant changes in the 3DOM architecture. The EDS map (Fig. 1b2) presents that the Ce element was well distributed, indicating that the CeO₂ particles were highly dispersed on the surface of 3DOM LaFeO₃.

The TEM images of xCeO₂/LaFeO₃ (Fig. 1c–e) show that CeO₂ nanoparticles (2–3 nm) were highly dispersed on the 3DOM LaFeO₃ surface for the 5%CeO₂/LaFeO₃ (Fig. 1c1 and c2) and 10%CeO₂/LaFeO₃ (Fig. 1e1 and e2) samples. While for the 20%CeO₂/LaFeO₃ (Fig. 1d1 and d2), some CeO₂ particles aggregated. The HRTEM image of a typical CeO₂ particle in the 10%CeO₂/LaFeO₃ sample and the corresponding Fourier transform image shows the CeO₂ grain with a fringe spacing of 0.19 nm corre-

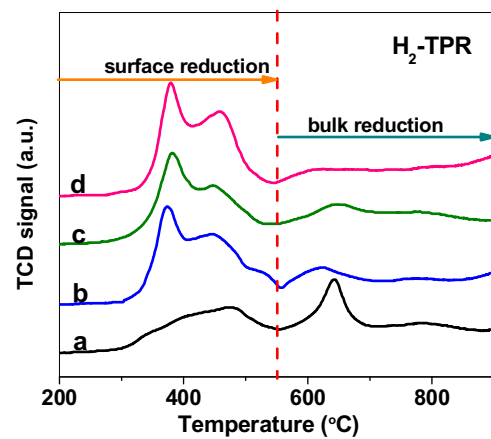


Fig. 2. H₂-TPR profiles of LaFeO₃ (a), 5%CeO₂/LaFeO₃ (b), 10%CeO₂/LaFeO₃ (c) and 20%CeO₂/LaFeO₃ (d).

sponding to (1 1 0) plane (Fig. 1f). The HRTEM image of LaFeO₃ in the 10%CeO₂/LaFeO₃ (Fig. 1g) indicates that the LaFeO₃ grain revealed a fringe spacing of 0.279 nm corresponding to (1 1 0) plane.

The reduction properties of the samples were evaluated using H₂-TPR, and the results are shown in Fig. 2. LaFeO₃ exhibited a series of overlapping reduction bands in the temperature range from 300 to 500 °C and a sharp peak with an onset temperature of 550 °C, which correspond to the two-step reduction (surface reduction and bulk reduction, respectively) of labile FeO_x phases [43–45]. The presence of CeO₂ on LaFeO₃ significantly modified the TPR profiles. The reduction peak at high temperature (higher than 550 °C) which can be observed over the pure LaFeO₃ sample nearly disap-

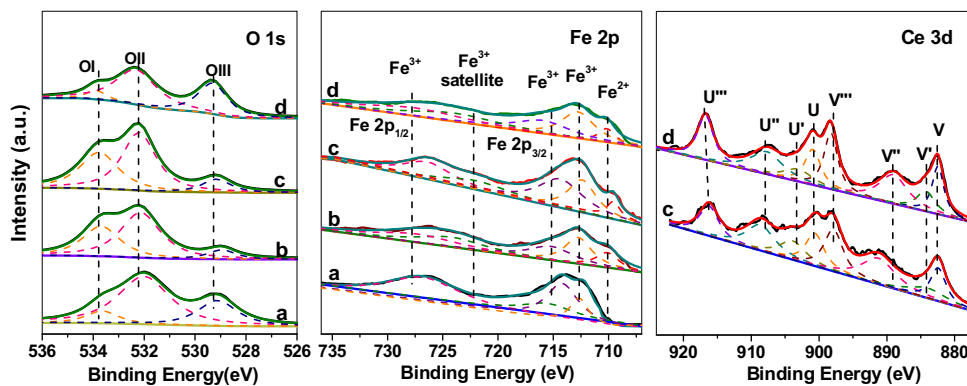


Fig. 3. O 1s, Fe 2p and Ce 3d spectra for LaFeO₃ (a), 5%CeO₂/LaFeO₃ (b), 10%CeO₂/LaFeO₃ (c) and 20%CeO₂/LaFeO₃ (d).

Table 1
XPS-derived characteristics for the xCeO₂/LaFeO₃ samples.

Oxygen Carriers	Oxygen species percentages (%)			O _{ads} /O _{latt} ratios	Fe iron percentages (%)		Fe ²⁺ /Fe ³⁺ ratios	Ce iron percentages (%)		Ce ³⁺ /Ce ⁴⁺ ratios
	OI	OII	OIII		Fe ²⁺	Fe ³⁺		Ce ³⁺	Ce ⁴⁺	
LaFeO ₃	10.1	64.1	25.8	2.87	0	100	0	—	—	—
5%CeO ₂ /LaFeO ₃	36.4	47.5	16.1	5.21	15	85	0.12	—	—	—
10%CeO ₂ /LaFeO ₃	37.1	52.8	10.1	8.90	11	89	0.17	21.2	79.8	0.27
20%CeO ₂ /LaFeO ₃	12.1	54.1	33.8	1.96	13	87	0.15	16.4	83.6	0.19

peared. The intensity of the reduction peaks at low temperatures (300–550 °C) was strongly enhanced. The enhanced reducibility at low temperatures suggests that oxygen located within the subsurface or bulk of the oxide can migrate to the surface immediately as surface oxygen was consumed, indicative of relatively high lattice oxygen mobility [41]. It should be stressed that the low-temperature peaks (300–550 °C) for the xCeO₂/LaFeO₃ samples must be mainly attributed to the reduction of FeO_x, although the isolated CeO₂ particles also contributed to this reduction process. Because virtually no noticeable increase in the intensity of the two peaks was observed when the CeO₂ content increased from 5% to 20% (see the curves b–d in Fig. 2). The results suggest that the interaction between CeO₂ and 3DOM LaFeO₃ could significantly improve the reducibility of LaFeO₃.

The surface elemental composition and chemical status of the samples were analysed using XPS technique. Fig. 3 shows the O 1s, Fe 2p and Ce 3d spectra of the pure LaFeO₃ and xCeO₂/LaFeO₃ samples. The atomic ratios of the surface species based on the corresponding fitted peaks are listed in Table 1. In the O 1s spectrum, three oxygen signals were observed at 533.8 (labelled as OI), 532.2 (labelled as OII) and 529.4 eV (labelled as OIII), which can be ascribed to hydroxyl and/or carbonate species on the surface (O_{ads}), surface absorbed oxygen (O_{ads}) and lattice oxygen (O_{latt}), respectively [46–48]. The O_{ads}/O_{latt} molar ratios over different samples exhibited the following sequence: 10%CeO₂/LaFeO₃ > 5%CeO₂/LaFeO₃ > LaFeO₃ > 20%CeO₂/LaFeO₃. Generally, the oxygen defect concentration over the CeO₂-based materials is proportional to the O_{ads}/O_{latt} ratio. The relatively higher O_{ads}/O_{latt} ratios over the 10%CeO₂/LaFeO₃ and 5%CeO₂/LaFeO₃ samples than the pure LaFeO₃ indicates that adding suitable amount of CeO₂ could enhance the formation of oxygen defects. This must be related to the chemical interaction between CeO₂ and LaFeO₃. For the 20%CeO₂/LaFeO₃ sample, the relatively low oxygen defect concentration should be attributed to the agglomeration of CeO₂ particles on the material (as observed by TEM measurement). The agglomerated CeO₂ particles are harmful to the CeO₂-LaFeO₃ interaction and may cover the defect sites on the LaFeO₃.

In the Fe 2p spectrum, three distinct peaks for Fe 2p_{1/2} (725.7 eV), Fe 2p_{3/2} (712.5 and 714.9 eV) and a shakeup satellite at 722.3 eV were observed for all of the samples, which are characteristic of Fe³⁺ ions [49]. In addition, a binding energy of ~709.7 eV corresponding to Fe²⁺ ions was also observed over all the xCeO₂/LaFeO₃ samples. In generally, Fe²⁺ is not stable in LaFeO₃ perovskite oxide. This indicates that the presence of CeO₂ nanoparticles on LaFeO₃ favours the formation of Fe²⁺ due to the CeO₂-LaFeO₃ interaction.

In the Ce 3d spectrum, the peaks labelled as V (V, V', V'' and V''') correspond to the Ce 3d_{5/2} contribution, and the peaks labelled as U (U, U', U'' and U'') represent the Ce 3d_{3/2} contribution. The V-U, V''-U'' and V'''-U''' doublets are assigned to Ce(IV) final states (Ce⁴⁺ ions), and the V' and U' peaks indicate the presence of Ce³⁺ ions [50]. The relative concentrations of Ce³⁺ and Ce⁴⁺ ions based on the XPS data were listed in Table 1. The 10%CeO₂/LaFeO₃ sample exhibited the highest concentration of Ce³⁺ and Fe²⁺ ions among the four samples. This suggests that it may own the most abundant oxygen vacancies because both of the coexistence of Fe²⁺ and Ce³⁺ ions which would induce the formation of oxygen defects.

Fig. 4 shows the CH₄-TPR profiles of pure LaFeO₃ and xCeO₂/LaFeO₃ samples. The reduction process for each sample can be divided into two distinct periods. First, CH₄ was converted to CO₂ and H₂O by the active oxygen (surface oxygen) in a temperature range of 550–650 °C. The amounts of produced CO₂ increased with CeO₂ content. In the second stage, large amounts of CO and H₂ were produced at temperatures higher than 700 °C due to the conversion of CH₄ to CO and H₂ by the less-active oxygen (lattice oxygen) [6,9]. For pure LaFeO₃, CO production began to decrease when the temperature reached to 870 °C, while the H₂ production continued to increase, leading to the H₂/CO ratio in the produced sygas higher than 2.0. This indicates the occurrence of methane decomposition, which must result in the formation of carbon deposition. By contrast, the H₂/CO ratio remained at around 2.0 until 900 °C for the 5%CeO₂/LaFeO₃ and 10%CeO₂/LaFeO₃ samples, indicating no formation of carbon deposition. This phenomenon suggests that the 5%CeO₂/LaFeO₃ and 10%CeO₂/LaFeO₃ samples had abundant oxygen species for the conversion of methane to CO and H₂. For the

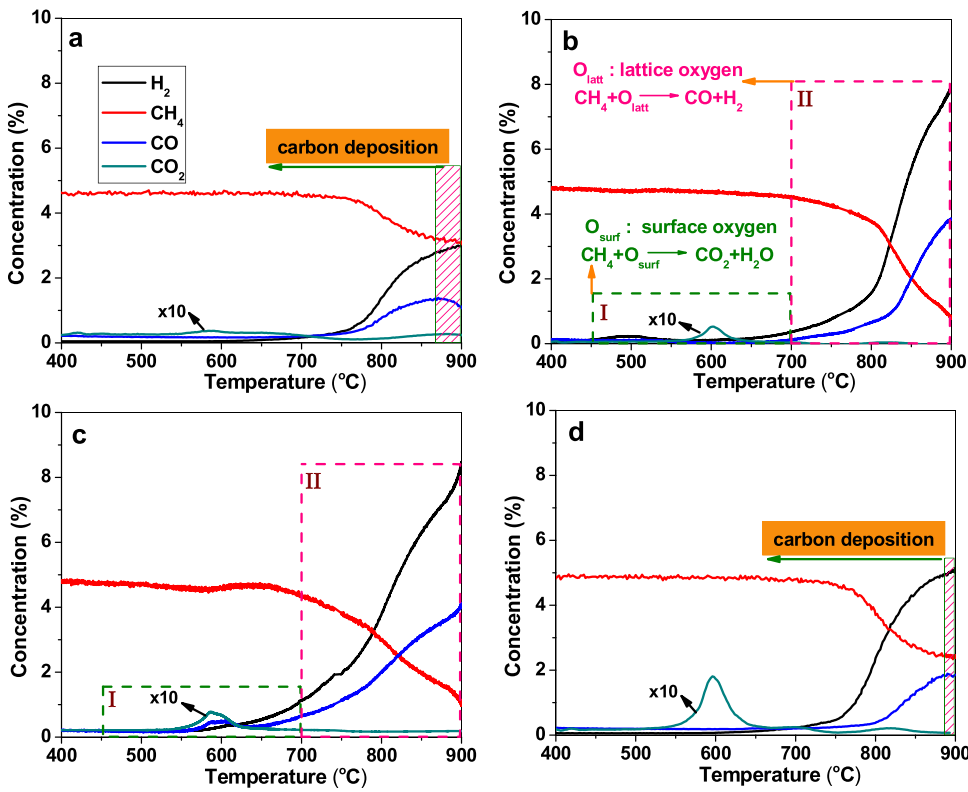


Fig. 4. CH₄-TPR results over pure LaFeO₃ (a), 5%CeO₂/LaFeO₃ (b), 10%CeO₂/LaFeO₃ (c) and 20%CeO₂/LaFeO₃ (d).

20%CeO₂/LaFeO₃ sample, it produced more CO₂ at low temperatures but less CO and H₂ at high temperatures.

The results shown in Fig. 4 suggest that carbon deposition can be minimized when methane reforming is performed at a temperature less than 850 °C. Therefore, a temperature of 800 °C was chosen for the isothermal reactions. Fig. 5 shows the gas components as well as the corresponding CH₄ conversion and CO selectivity during the CH₄ pulse reactions at 800 °C. At the beginning of the reaction, a large amount of CH₄ was converted to CO₂, and only a small amount of CO and H₂ was detected, leading to a lower CO selectivity (Fig. 5 a2-d2). Then, the amount of CO₂ decreased quickly to the baseline, and the CO and H₂ amounts increased as the pulse number rising. In comparison to pure LaFeO₃, all of the CeO₂/LaFeO₃ samples exhibited higher CH₄ conversions. Among the three CeO₂/LaFeO₃ samples, 10%CeO₂/LaFeO₃ exhibited the highest CH₄ conversion, which is in agreement with the CH₄-TPR results (Fig. 4).

The available OSC and percentage of oxygen recovery, which were calculated from the results of the CH₄ and O₂ pulse reactions, are shown in Fig. 6A. The available OSC is defined as the maximum amount of oxygen in oxygen carriers consumed by methane reduction without the formation of carbon deposition. The amount of oxygen consumed was higher than the oxygen stored due to an irreversible removal of surface oxygen species [51]. The available OSC and percentage of oxygen recovery were the highest for 10%CeO₂/LaFeO₃ and the lowest for LaFeO₃. This should be related to the superior oxygen mobility and high concentration of oxygen vacancies resulting from the interaction between CeO₂ and LaFeO₃, which favour the removal and replenishment of lattice oxygen [52].

The corresponding available OSC calculated from the successive reduction/oxidation pulse reactions is shown in Fig. 6B. The available OSC of LaFeO₃ is in a range of 2.39–2.48 mmol g⁻¹ (i.e., 2.44 mmol g⁻¹ on average) during the 10 pulse cycles, while the OSC of 10%CeO₂/LaFeO₃ slightly changes from 3.71 to 3.79 mmol g⁻¹ (3.75 mmol g⁻¹ on average). This result indicates that the reduc-

tion/oxidation cycles do not decrease the available OSC of either LaFeO₃ or 10%CeO₂/LaFeO₃ sample, suggesting relatively high chemical stability.

Fig. 7 shows the CH₄-TPD profiles for different samples. For the pure LaFeO₃ (Fig. 7a), limited CO₂, CO and H₂ originating from the reaction between adsorbed methane and surface oxygen species on the oxygen carrier were detected in a temperature range of 360–750 °C. However, a large amount of CO₂ was observed over the fresh 10%CeO₂/LaFeO₃ (Fig. 7b), and almost no CO or H₂ was detected. Since the CO₂ can only come from the oxidation methane, this suggests that more methane molecules were adsorbed on the 10%CeO₂/LaFeO₃ sample. The relatively high concentration of adsorbed oxygen (as observed by the XPS and CH₄-TPR measurements) is favourable for the conversion of CH₄ to CO₂. When 10%CeO₂/LaFeO₃ sample was suffered one redox cycle, the signal of CO₂ almost disappeared, and a large number of CO and H₂ were detected. This indicates that most of the adsorbed oxygen species, which result in the formation of CO₂, were not restored in the re-oxidation step. It should be highlighted that the lattice oxygen in 10%CeO₂/LaFeO₃ is active enough to reaction with methane to produce CO and H₂.

The successive chemical looping reaction was also performed over the LaFeO₃ and 10%CeO₂/LaFeO₃ oxygen carriers at 800 °C. The CO selectivity and syngas yield during the multi-cyclic were calculated based on the original experiment data, as shown in Fig. 8. It can be seen that the CO selectivity either for LaFeO₃ or 10%CeO₂/LaFeO₃ sample maintained at ca. 90% during the 30 successive redox cycles. The syngas yield over the LaFeO₃ sample increased from 5.34 mmol g⁻¹ to 5.97 mmol g⁻¹ during the first five cycles. Thereafter, it slightly decreased with the redox experiment proceeding. However, the syngas yield increased again after 20 cycles. It is noted that the H₂/CO ratio in the produced syngas also increased in the later period of the cycling, and it reached to 2.45 after 30 redox cycles. Since the stoichiometric reaction of a

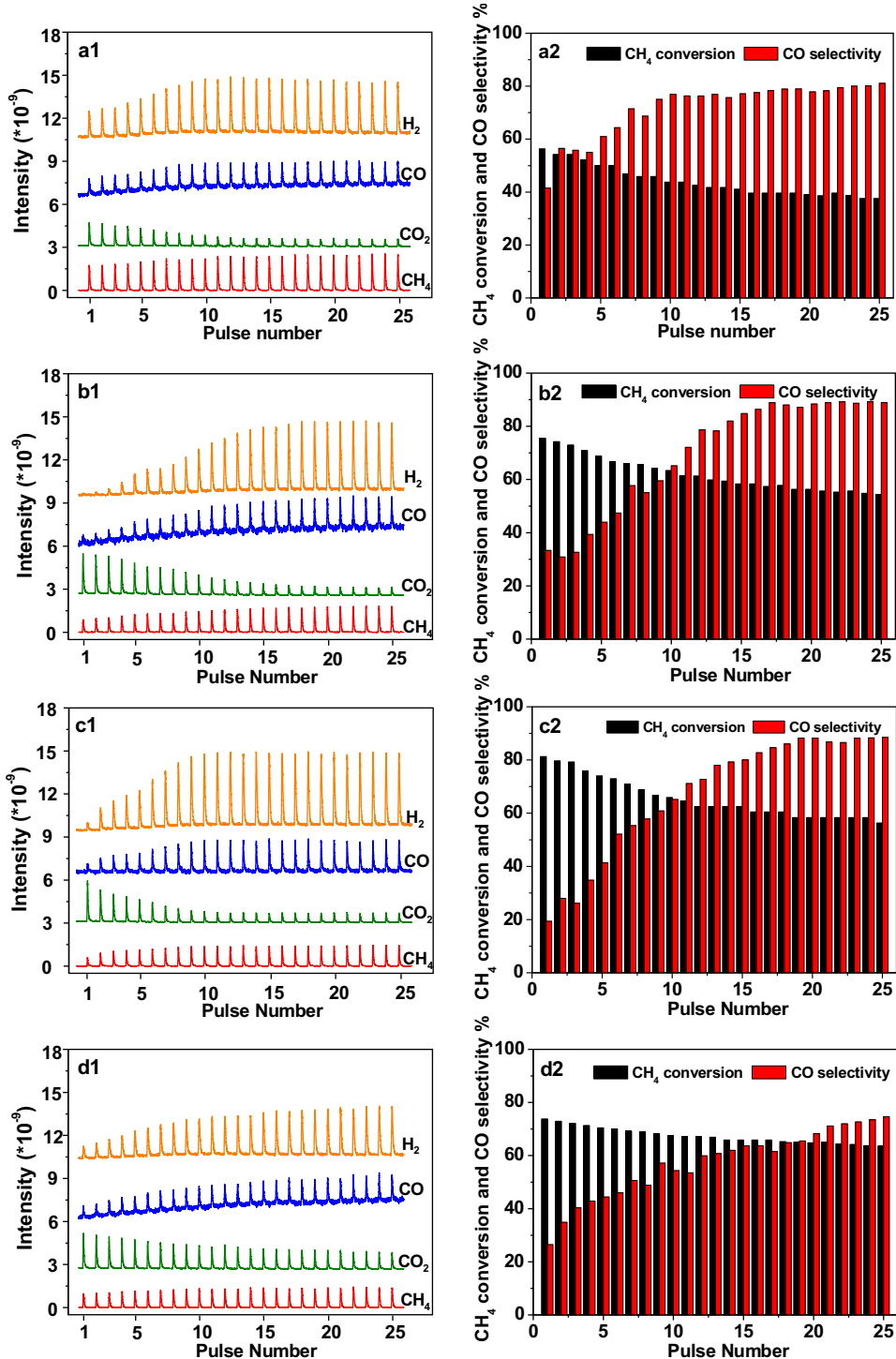


Fig. 5. Gas components, CH₄ conversion and CO selectivity during CH₄ pulses at 800 °C over pure LaFeO₃ (a1, a2), 5%CeO₂/LaFeO₃ (b1, b2), 10%CeO₂/LaFeO₃ (c1, c2) and 20%CeO₂/LaFeO₃ (d1, d2) samples.

CH₄ molecule with oxygen should yield a H₂/CO ratio of 2.0, ratios higher than 2.0 indicates the decomposition of CH₄ which would result in the formation of carbon deposition. In general, for the reaction of methane with oxygen carriers, methane is first activated to form carbon intermediates, and the carbon can be quickly removed when the surface of oxygen carriers is rich in active oxygen. As observed in Fig. 8a, the reducibility of pure LaFeO₃ is reduced by the redox treatment, resulting in relatively lower concentration of active oxygen. In this case, the formation of carbon deposi-

tion during the redox cycling must be attributed to the weakened reducibility of the oxygen carrier. For the 10%CeO₂/LaFeO₃ sample, the syngas yield (with an average value of 9.94 mmol g⁻¹) is much higher than that over the pure LaFeO₃, and it is very stable during the redox testing. More importantly, it maintained a H₂/CO ratio near the theoretical 2.0 value (i.e., 1.99–2.04) in the whole redox experiment. The formation of carbon deposition is avoided. This suggests that the combination of 3DOM LaFeO₃ with CeO₂ nano particles could enhance both the activity for chemical looping con-

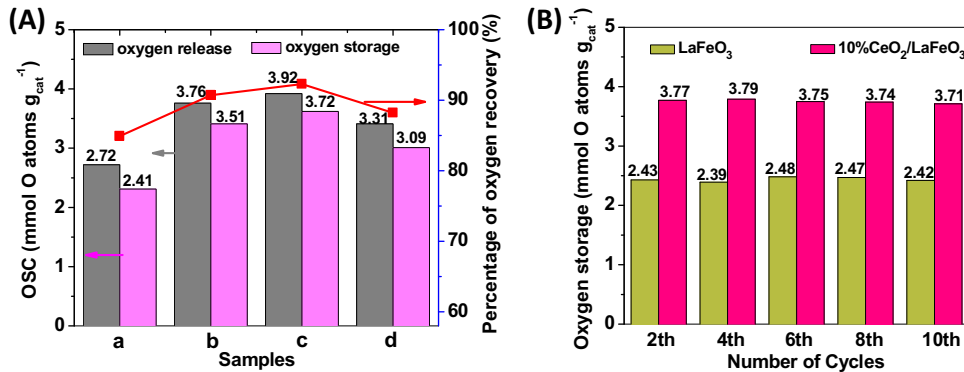


Fig. 6. (A) The OSC and percentage of oxygen recovery over reduced LaFeO₃ (a), 5%CeO₂/LaFeO₃ (b), 10%CeO₂/LaFeO₃ (c) and 20%CeO₂/LaFeO₃ (d). (B) The oxygen storage for 10 cycles of O₂ pulse reactions at 800 °C over reduced LaFeO₃ and 10%CeO₂/LaFeO₃.

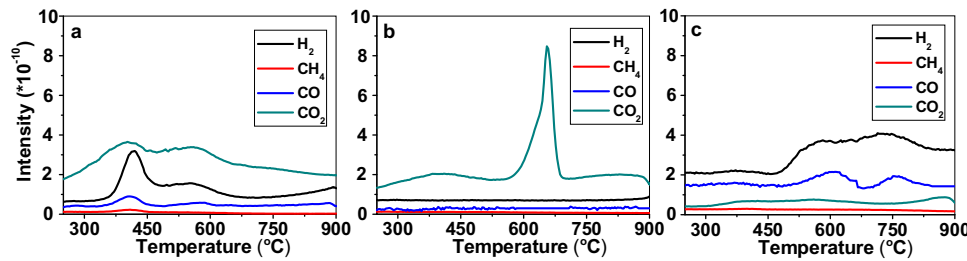


Fig. 7. CH₄-TPD profiles of fresh LaFeO₃ (a), fresh 10%CeO₂/LaFeO₃ (b) and re-oxidized 10%CeO₂/LaFeO₃ sample (c).

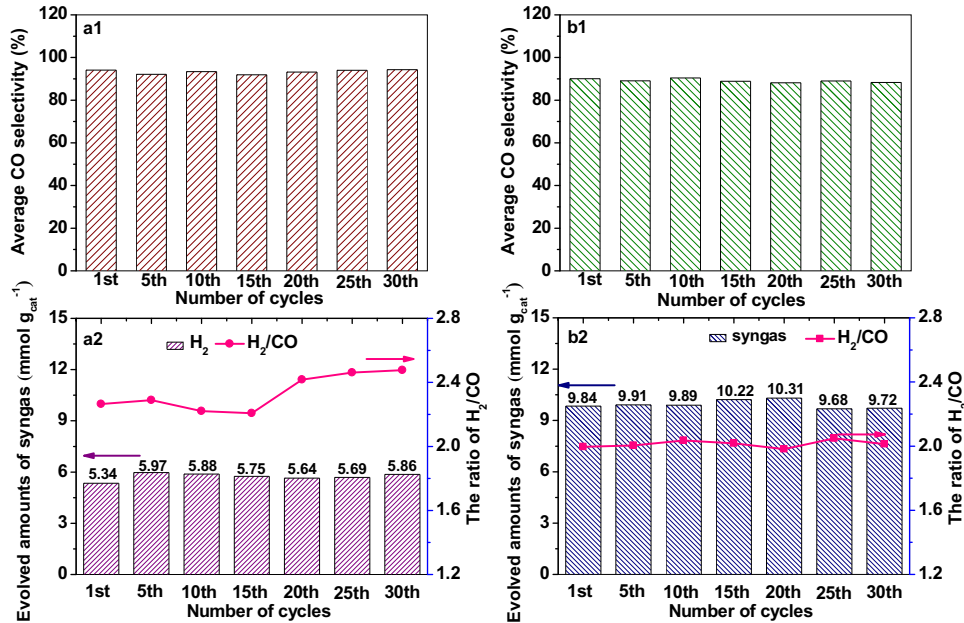


Fig. 8. CO selectivity and syngas yield during the chemical looping reforming of methane over LaFeO₃ (a1, a2) and 10%CeO₂/LaFeO₃ (b1, b2).

version of methane to syngas and the resistance towards carbon formation.

The water splitting reaction was also performed on the reduced samples for pure hydrogen generation. To investigate the effect of temperature on the reactivity of oxygen carriers, the reaction was performed at 600 and 800 °C, respectively. The results are shown in Fig. 9A. As can be seen, both CO and H₂ were detected for the LaFeO₃ sample. The major product (H₂) originated from water reacting with the reduced LaFeO₃. The formation of CO must be due

to the steam gasification of carbon deposition (C + H₂O → CO + H₂), evidencing the appearance of carbon deposition after the previous CH₄ isothermal reaction. More CO was produced at 800 °C compared to that at 600 °C because a high temperature is beneficial for the oxidation of carbon. This also suggests that the carbon deposition cannot be totally removed by the steam at 600 °C. By contrast, no CO was detected over the reduced 10%CeO₂/LaFeO₃ sample either at 600 °C or at 800 °C, indicating no carbon deposition on this sample. Among the four samples, the sequence of the syngas yield

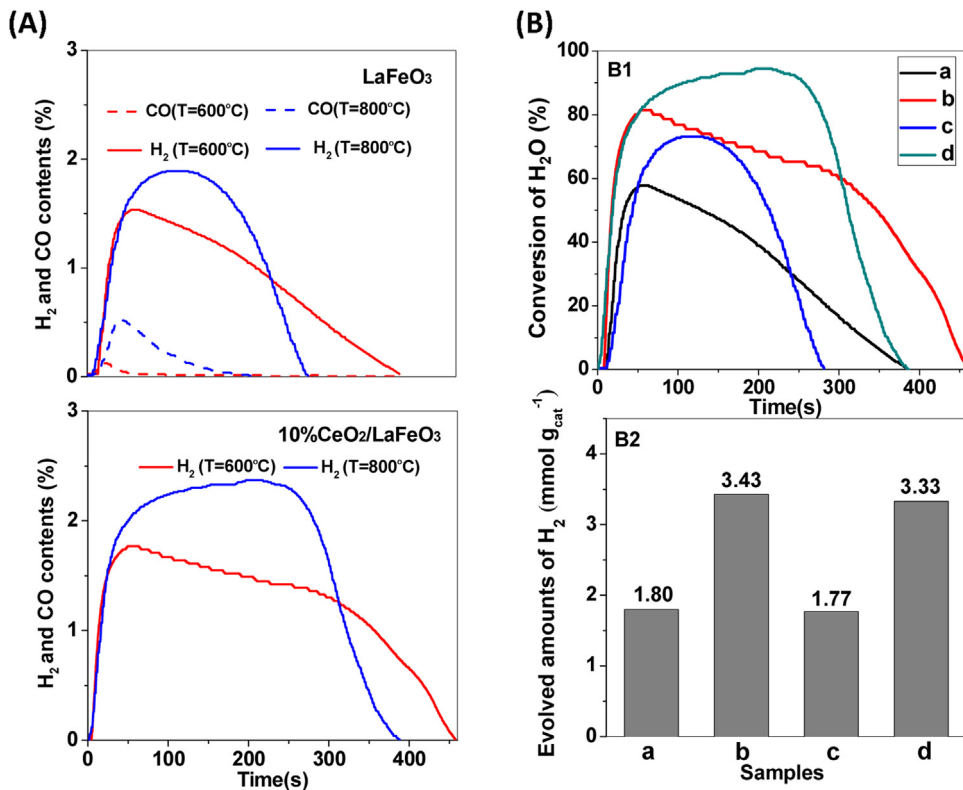


Fig. 9. (A) Evolved amounts of H₂ and CO in the water splitting reaction at different reaction temperatures over reduced LaFeO₃ and 10%CeO₂/LaFeO₃. (B) Conversion of H₂O (B1) and evolved amounts of H₂ (B2) in the water splitting reaction at different reaction temperatures over reduced LaFeO₃ (a: T = 600 °C; c: T = 800 °C) and 10%CeO₂/LaFeO₃ (b: T = 600 °C; d: T = 800 °C).

is as follow: 10% CeO₂/LaFeO₃ (9.84 mmol g⁻¹) > 5% CeO₂/LaFeO₃ (9.13 mmol g⁻¹) > 20% CeO₂/LaFeO₃ (7.52 mmol g⁻¹) > LaFeO₃ (5.34 mmol g⁻¹).

Fig. 9B shows the corresponding conversion of H₂O and H₂ yield over different samples. For 10%CeO₂/LaFeO₃, when the reaction was performed at 800 °C, the average conversion of H₂O was higher than that at 600 °C because that the high temperature can enhance the reaction rate of H₂O splitting. In addition, the average conversion of H₂O over 10%CeO₂/LaFeO₃ was higher than that over LaFeO₃ when the reaction was performed at either 600 or 800 °C. The average conversion of H₂O over 10%CeO₂/LaFeO₃ at 800 °C was close to 90%, while the average conversion of H₂O over LaFeO₃ was only 70%. As shown in Fig. 9B2, the H₂ yield over the reduced 10%CeO₂/LaFeO₃ was 3.43 and 3.33 mmol g⁻¹ at 600 and 800 °C, respectively. On the other hand, the evolved amounts of H₂ over the reduced LaFeO₃ were only 1.77 and 1.80 mmol g⁻¹ at 600 and 800 °C, respectively. The hydrogen yield over the 10%CeO₂/LaFeO₃ sample is almost twice that over the pure LaFeO₃ sample. This suggests that the presence of CeO₂ on LaFeO₃ significantly enhanced the content of reversible oxygen in the oxygen carrier for hydrogen generation via the CLRM technology.

To determine the performance for successive production of hydrogen over the oxygen carriers, 30 repetitive cycles of the CLRM process were performed and the results were shown in Fig. 10. Both H₂ and CO were detected in the redox process over the LaFeO₃ samples, and no obvious decrease in the hydrogen quantities was observed as the cycle number increased. The formation of CO in the water splitting reaction indicates the presence of carbon deposition during the CH₄ oxidation. By contrast, no CO was detected over the 10%CeO₂/LaFeO₃ in the redox process, indicating high resistance towards carbon formation. In addition, 10%CeO₂/LaFeO₃ sample also showed high stability during the cycling. In summary, the presence of CeO₂ on 3DOM LaFeO₃ results in good reactivity,

high hydrogen yields and superior carbon deposition resistance for the successive CLRM cycles.

The effect of the redox cycling on the structural stability and reducibility of the oxygen carriers was also investigated. Fig. 11A shows the XRD patterns of fresh and recycled LaFeO₃ and 10%CeO₂/LaFeO₃ sample. XRD characterization revealed that LaFeO₃ with a perovskite structure (JCPDS card [37-1493]) was obtained either for the pure LaFeO₃ or the 10%CeO₂/LaFeO₃ sample. Weak diffraction peaks for CeO₂ were also presented over fresh and recycled 10%CeO₂/LaFeO₃ samples. No obvious evolution on the structure of the two materials was observed after the long term cycling at 800 °C. This suggests that the effect of redox treatment on the crystal structure of 10%CeO₂/LaFeO₃ sample is not significant.

The H₂-TPR profiles of fresh and recycled LaFeO₃ and 10%CeO₂/LaFeO₃ oxygen carrier are presented in Fig. 11B. It can be seen that the reduction behaviors of the pure LaFeO₃ sample significantly changed after the redox cycling. The reduction peaks for the recycled LaFeO₃ sample shifted to higher temperature and their intensity obviously decreased, indicating weaker reducibility. By contrast, no obvious evolution on the TPR profile of the 10%CeO₂/LaFeO₃ sample is observed after cycling. This suggests that the presence of CeO₂ strongly improved the redox stability of LaFeO₃ material.

Fig. 12 shows the O 1s and Fe 2p XPS patterns of recycled LaFeO₃ and 10%CeO₂/LaFeO₃ samples. The atomic ratios of the surface species based on the corresponding fitted peaks were listed in Table 2. The recycled samples also revealed three oxygen species (OI, OII and OIII), which are associated with hydroxyl and/or carbonate species on the surface, surface absorbed oxygen and lattice oxygen, respectively [46–48]. Compared with the fresh samples (see the data in Table 1), the O_{ads}/O_{latt} molar ratio either for LaFeO₃ or 10%CeO₂/LaFeO₃ decreased, which indicates that some surface oxygen species were removed after the redox cycling. It

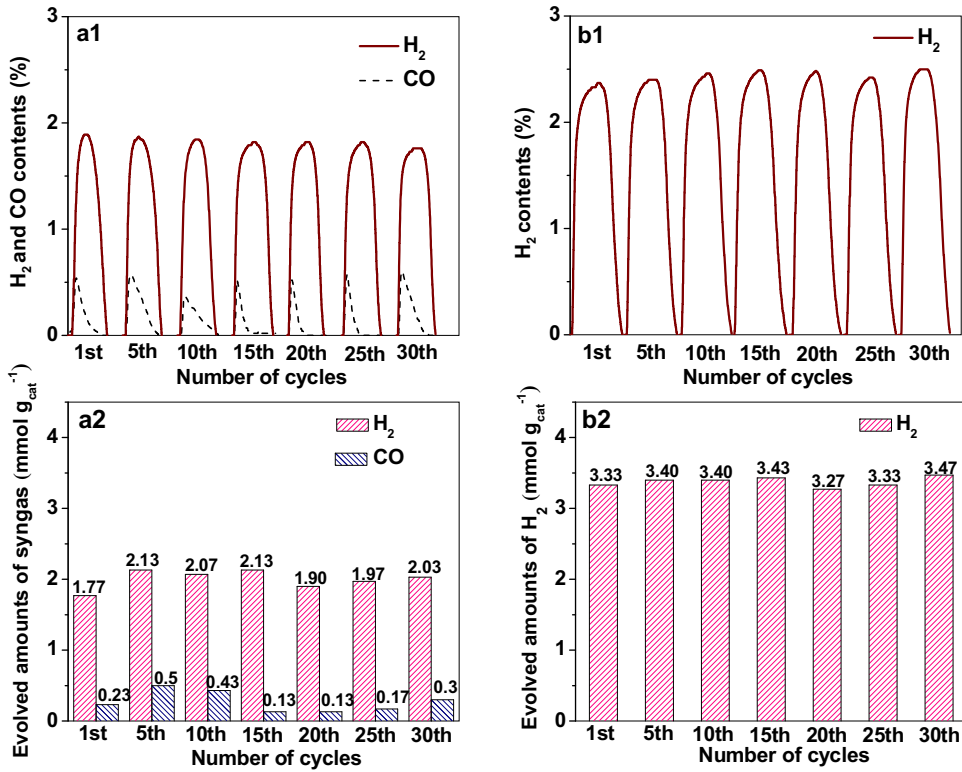


Fig. 10. Contents and evolved amounts of H_2 and CO for the water splitting reactions during the 30 CLRM cycles at $800\ ^\circ C$ over LaFeO_3 (a1, a2) and 10% $\text{CeO}_2/\text{LaFeO}_3$ (b1, b2) samples.

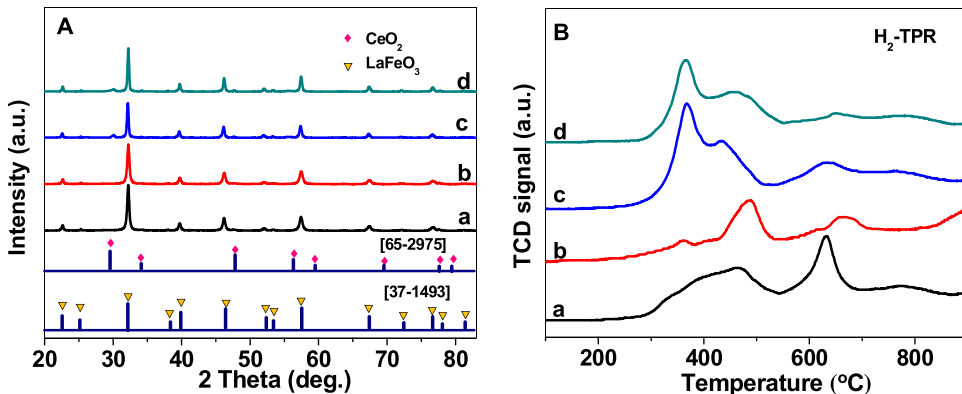


Fig. 11. Comparison of XRD (A) and H_2 -TPR (B) patterns over fresh LaFeO_3 (a), LaFeO_3 after 30 successive redox cycles (b), fresh 10% $\text{CeO}_2/\text{LaFeO}_3$ (c) and 10% $\text{CeO}_2/\text{LaFeO}_3$ after 30 CLRM cycles (d).

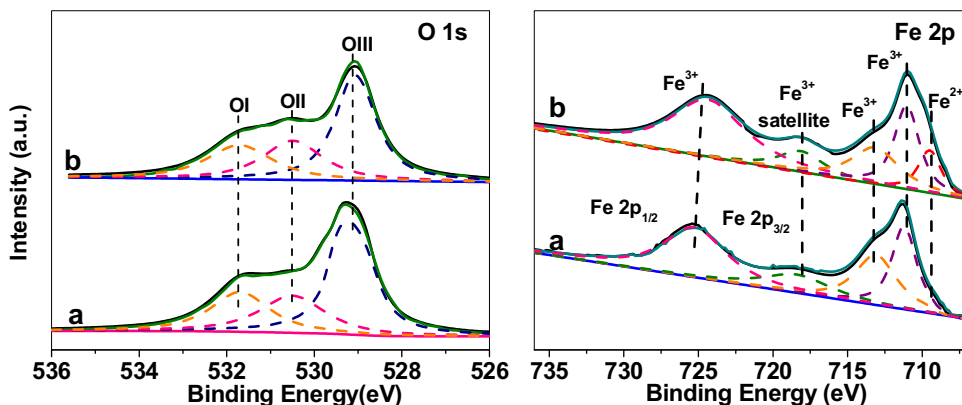


Fig. 12. Comparison of XPS patterns over LaFeO_3 (a) and 10% $\text{CeO}_2/\text{LaFeO}_3$ (b) after 30 CLRM cycles.

Table 2XPS-derived characteristics for the recycled LaFeO₃ and 10%CeO₂/LaFeO₃ samples.

Oxygen Carriers	Oxygen species percentages (%)			O _{ads} /O _{latt} ratios	Fe iron percentages (%)		Fe ²⁺ /Fe ³⁺ ratios
	OI	OII	OIII		Fe ²⁺	Fe ³⁺	
LaFeO ₃	23.6	24.3	52.1	0.91	0	100	0
10%CeO ₂ /LaFeO ₃	26.1	27.4	46.5	1.15	9	91	0.099

should be stressed that the O_{ads}/O_{latt} molar ratio over the recycled 10%CeO₂/LaFeO₃ is still higher than that over the recycled LaFeO₃ sample. For the Fe 2p spectra, three distinct peaks for Fe 2p_{1/2}, Fe 2p_{3/2} and a shakeup satellite were observed for both the two samples, which are characteristic of Fe³⁺ ions. It should be highlighted that the binding energy of ~709 eV corresponding to Fe²⁺ ions still can be detected for the recycled 10%CeO₂/LaFeO₃ sample. This indicates that the strong interaction between CeO₂ nanoparticles and LaFeO₃, which result in the formation of Fe²⁺, still existed even after 30 successive redox cycles.

4. Discussion

4.1. Oxygen species and oxygen vacancy

Dai et al. [9,10] proposed that two types of oxygen species exist on or in LaFeO₃. The oxygen species can be defined as very reactive oxygen species for CO₂ formation and less reactive oxygen species for CO and H₂ formation. The concentration of highly reactive oxygen, which is identified as the loosely bound adsorbed surface oxygen, is relatively low. The less reactive oxygen species, which is the major oxygen species in the LaFeO₃, is due to lattice oxygen [10,53]. Mihai et al. [11] also suggested that CO₂ can only be formed on the surfaces with a high surface O concentration or site coverage at the Fe sites associated with high surface O atoms. Mudu et al. [53] reported that the concentration of active oxygen species affects CH₄ conversion, and lattice oxygen plays a key role in controlling the CO selectivity. These conclusions agree with the results from our experiments. Therefore, the fresh CeO₂/LaFeO₃ samples exhibit high methane conversion but relatively low CO selectivity, as shown in Fig. 5. Dai et al. [9,10] also proposed that the oxygen species in LaFeO₃ for CO formation can be recovered but the reactive oxygen species for CO₂ formation is barely restored at the appropriate conditions. A very interesting approach to improve the selectivity of syngas was also performed by controlling the amount of oxygen re-injected into the reduced LaFeO₃ [11]. The CH₄-TPD measurement suggested the removal of the surface active oxygen by the partial re-oxidation process (see Fig. 7c). These results support the previous observations that the reduced lattice oxygen is first restored in the re-oxidation step, followed by the recovery of the surface active oxygen. Since the activity of H₂O is much lower than O₂, the water splitting reaction could selectively restore the oxygen in the bulk of the oxygen carrier. This could improve the selectivity of syngas over re-oxidized oxygen carriers.

Oxygen vacancy sites on the surface of oxygen carriers are generally generated by removal of O atoms [11]. Surface oxygen vacancies are proposed to participate in many chemical reactions catalyzed by metal oxides via a Mars/van Krevelen mechanism [18]. Deng et al. [54] reported that the generation of oxygen vacancies on the perovskite-type catalyst facilitates the activation of adsorbed oxygen molecules and enables the replenishment of surface oxygen species. For CeO₂, the oxygen vacancies are identified as potent surface sites for reactant adsorption and subsequent activation [55]. In addition, the formation of oxygen vacancies would also provide pathways for oxygen transports through the bulk lattice for surface reaction [56]. It is proposed that, in the reaction between methane and CeO₂, methane was activated on the Ce³⁺

sites (which are associated with the oxygen vacancies) to form carbon intermediates and that CO was produced by the reaction of carbon with lattice oxygen [19]. Methane oxidation on perovskite-type catalysts is an example of an interfacial process where the increased oxygen mobility dominates catalytic activity, and both the oxygen vacancy and the undercoordinated metal cations play a significant role for the gas-solid reaction [57]. Either for CeO₂ or perovskite-type oxides, higher concentration of oxygen vacancies could enhance their reducibility [9,11,34]. In the re-oxidation step, the presence of oxygen vacancies also plays an important role, because it can accelerate the mobility of oxygen from the surface to the bulk [36].

The addition of oxides to perovskite-type could modify the concentration of oxygen vacancies. Zhang et al. [31] reported that the coupling of Mn⁴⁺/Mn³⁺ and Ce⁴⁺/Ce³⁺ couples in the LaMnO₃/CeO₂ system strongly enhance the redox capacity of the surface species, due to the higher concentration of oxygen vacancy. Li et al. [15–17] prepared a series of Fe₂O₃@La_{0.8}Sr_{0.2}FeO_{3-δ} core–shell oxygen carriers, which exhibited high activity and selectivity for the conversion of methane to syngas via a chemical looping process. The improved activity can be attributed to smaller nanoscale Fe₂O₃ cores, which provide more readily accessible lattice oxygen through the mixed conductive shell where abundant oxygen vacancy may exist. In the present work, the interaction between CeO₂ and LaFeO₃ was also detected. The XPS results (see Fig. 3 and Table 1) indicate the presence of Fe²⁺ due to the addition of CeO₂. Moreover, Ce³⁺ was also detected on the CeO₂/LaFeO₃ samples. The coexistence of Fe²⁺ and Ce³⁺ ions would improve the formation of oxygen vacancies due to the charge balance. The high concentration of oxygen vacancies results in the obviously enhancement on the reducibility and oxygen mobility of CeO₂/LaFeO₃ samples, as observed by H₂-TPR (see Fig. 2). The 10%CeO₂/LaFeO₃ oxygen carrier with the most abundant Fe²⁺ and Ce³⁺ ions has the highest activity for methane oxidation in the reduction step. Also, it further increased the hydrogen yield in the water splitting step due to the relatively high reduction extent.

4.2. Carbon deposition

Carbon deposition is a serious issue in the CLRM technology, because the presence of carbon deposition would reduce the purity of produced hydrogen in the water splitting step. For the reaction between methane and oxygen carriers, methane should be first activated on the oxygen carriers and then the activated methane reacts with lattice oxygen to form CO and H₂ [11,19,23]. The formation of syngas depends on the matching between the activation rate of methane and the mobility of lattice oxygen. The lack of lattice oxygen or poor oxygen mobility would result in the formation of carbon deposition. Mihai et al. [11] observed that the carbon deposition formed over LaFeO₃ as early as the formation of CO in the gas products and it became significant when almost half of the reducible oxygen was consumed. This suggests that the activation rate of methane over the LaFeO₃ should be higher than the removal rate of carbon deposition by lattice oxygen. The results in the present work also support this observation. As shown in Fig. 10, the formation of CO was detected in the water splitting reaction over the reduced pure LaFeO₃ sample with an oxygen consumption of 2.27 mmol g⁻¹, indicative of the formation of carbon deposition.

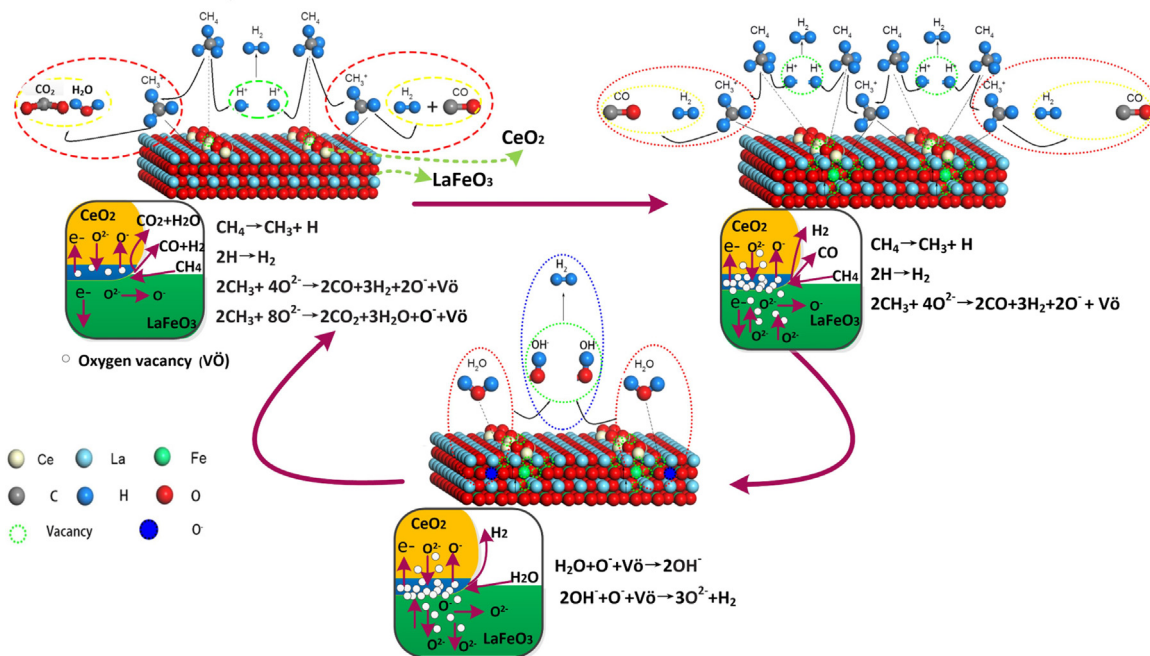


Fig. 13. Reaction mechanism model for CLRM over $\text{CeO}_2/\text{LaFeO}_3$ oxygen carriers.

The presence of CeO_2 on the surface of LaFeO_3 totally changed this situation. CeO_2 with good electronic and ionic conductivity modifies the reduction of LaFeO_3 . No CO or CO_2 was observed over the reduced 10% $\text{CeO}_2/\text{LaFeO}_3$ sample in the water splitting reaction, even the oxygen consumption reached to 3.38 mmol g^{-1} . This can be attributed to the enhanced oxygen mobility of LaFeO_3 due to the presence of CeO_2 , as observed in $\text{H}_2\text{-TPR}$ (see Fig. 2). The high resistance towards carbon formation allows the $\text{CeO}_2/\text{LaFeO}_3$ oxygen carrier provide more lattice oxygen for methane oxidation, which results in high H_2 yield in the water splitting step (nearly twice compared with that over the pure LaFeO_3).

4.3. Reaction mechanism

Based on the above discussions, the reaction mechanism model for CLRM over $\text{CeO}_2/\text{LaFeO}_3$ is proposed, as shown in Fig. 13. For a gas-solid reaction, both the surface and subsurface property of oxygen carrier are important. On the surface, the oxygen carrier must provide active sites for the adsorption and activation of the reactant molecules. Thereafter, the channels in the subsurface of oxygen carrier for the movement of activated reactant molecules or lattice oxygen control the reaction rate. In the absence of precious metal catalysts, oxygen vacancies (VO) as well as the resulting Fe^{2+} or Ce^{3+} ions, are identified as the active sites for methane activation. In the beginning of the reaction, the surface oxygen vacancies mainly play a relevant role for the adsorption and activation of the reactant molecules. When numbers of surface and subsurface oxygen was consumed, the undercoordinated metal cations (Fe^{2+} and Ce^{3+}) behave more metallic like and act as active centers for C–H dissociation. Alternatively, electrophilic oxygen that can evolve from the bulk may also contribute to C–H bond breaking. In this case, the coupling of undercoordinated metal cations with the abundant oxygen vacancies plays the most important role in the gas-solid reaction.

In the $\text{CeO}_2/\text{LaFeO}_3$ system, both Fe^{2+} and Ce^{3+} ions were detected due to the $\text{CeO}_2\text{-LaFeO}_3$ interaction and they should coexist in the interface between CeO_2 nano particles and LaFeO_3 . Such interfaces must possess abundant oxygen vacancies due to the

formation of undercoordinated metal cations, which will provide the active sites for methane adsorption. As reported, C–H bond in methane can be activated on VO rich interface, via homolytic hydrogen abstraction steps that form CH_3 groups with significant radical character and weak interactions with the surface at the transition state [58]. CO_2 is first formed when the most reactive oxygen species are consumed by the activated methane. For the further reduction of oxygen carriers to take place, there must be a transport of oxygen from the subsurface of LaFeO_3 to the interface. CO and H_2 increasingly become the main products. During the successive reacting with methane, the interface will be more and more depleted for oxygen and the oxygen will be supplied by bulk diffusion from the crystal lattice of LaFeO_3 . Since the $\text{CeO}_2\text{-LaFeO}_3$ interface possesses the most abundant oxygen vacancies, there should be a natural concentration gradient of oxygen vacancies around the interface sites. This concentration gradient would provide the pathways and energy for lattice oxygen diffusion, which leads to the enhancement on oxygen diffusivity. Finally, a great number of oxygen is taken out of the $\text{CeO}_2/\text{LaFeO}_3$ oxygen carriers by methane, which generates large amounts of syngas.

For the water splitting reaction, the O in the H_2O molecule would be taken by a more active cation in the oxygen carrier, along with the generation of H_2 . This process consists both in the adsorption of H_2O in the active sites and the dissociation of H_2O to recharge the iron cations in the reduced oxygen carriers. The above discussions suggest that the $\text{CeO}_2\text{-LaFeO}_3$ interface affects the activation of methane and that the bulk oxygen would transport to the interface by diffusion or spillover. The regeneration process in water stream is not necessary through the reverse oxygen transport as observed with methane, but can probably also occur directly with the interface due to the most abundant oxygen vacancy there. Generally, H_2O undergoes decomposition on the oxygen vacancies, reacting with adjacent O^- species, forming OH^- first [59,60]. Then O^{2-} ions form to restore the metal cations via the reforming of couple OH^- ions, accompanied by the generation of H_2 . After the supplement of oxygen species by H_2O , the oxygen carrier could continue to react with CH_4 . In this redox cycle, the syngas and hydrogen could be successively coproduced.

5. Conclusions

3DOM CeO₂/LaFeO₃ samples with different CeO₂ loadings were successfully prepared using a gas-bubble-assisted method. CeO₂ particles can be well dispersed on the 3DOM LaFeO₃ surface when the CeO₂ loading is lower than 20%. The presence of CeO₂ induces the formation of Fe²⁺ in LaFeO₃, which favours the formation of oxygen vacancies, strongly improving the reducibility, oxygen mobility and reactivity for methane oxidation. The available OSC, which is defined as the maximum amount of oxygen consumed by methane reduction without the formation of carbon deposition, increases from ca. 2.44 mmol g⁻¹ to ca. 3.75 mmol g⁻¹ due to the presence of CeO₂. During the CLRM process, the 10%CeO₂/LaFeO₃ reveals the highest yields of syngas (9.94 mmol g⁻¹) and pure hydrogen (3.38 mmol g⁻¹), which are much higher than that over the pure LaFeO₃ sample (5.73 mmol g⁻¹ for syngas and 2.00 mmol g⁻¹ for hydrogen). After 30 successive redox cycles, no decrease in the H₂ and syngas yields was observed over the 10%CeO₂/LaFeO₃ sample, indicating that such oxygen carrier is excellent for the CLRM technology.

The strong enhancement on the reactivity of CeO₂/LaFeO₃ oxygen carriers for methane oxidation and water splitting can be attributed to the CeO₂–LaFeO₃ interaction. Due to the coexistence of Ce⁴⁺–Ce³⁺ and Fe³⁺–Fe²⁺ couples on the interface between LaFeO₃ and CeO₂ particles, such interfaces must possess abundant oxygen vacancies, providing the active sites for methane adsorption and activation. There should be a natural concentration gradient of oxygen vacancies around the interface sites. With the reaction proceeding, the concentration gradient must be enhanced, which will broaden the pathways and supply sufficient energy for oxygen transport through the lattice towards the surface. The high oxygen diffusivity could inhibit the formation of carbon deposition and improve the reduction extent. This is beneficial to obtain high yields of syngas and hydrogen. The findings in the present work suggest that the design of efficient oxygen carriers for CLRM must consider the balance among the concentration of active sites for recants activation, the oxygen diffusivity and the available OSC.

Acknowledgements

This work has been financially supported by the National Natural Science Foundation of China (Project Nos. 51374004 and 51306084), the Candidate Talents Training Fund of Yunnan Province (Project Nos. 2014HB006 and 2012HB009), Scientific and Technological Leading Talent Projects in Yunnan Province (No. 2015HA019) and the Applied Basic Research Program of Yunnan Province (Project Nos. 2014FB123).

Appendix A. Supplementary data

Supplementary data associated with this article can be found, in the online version, at <http://dx.doi.org/10.1016/j.apcatb.2016.08.024>.

References

- [1] H.L. Chen, H.M. Lee, S.H. Chen, Y. Chao, M.B. Chang, *Appl. Catal. B* 85 (2008) 1–9.
- [2] Z.W. Li, M. Li, Z.F. Bian, Y. Kathiraser, S. Kawi, *Appl. Catal. B* 188 (2016) 324–341.
- [3] M. Keller, H. Leion, T. Mattisson, *Appl. Catal. B* 183 (2016) 298–307.
- [4] M.C. Tang, L. Xu, M.H. Fan, *Appl. Energy* 151 (2015) 143–156.
- [5] L. Nalbandian, A. Evdou, V. Zaspalis, *Int. J. Hydrogen Energy* 36 (2011) 6657–6670.
- [6] X. Zhu, Y.G. Wei, H. Wang, K.Z. Li, *Int. J. Hydrogen Energy* 38 (2013) 4492–4501.
- [7] M. Ortiz, L.F. Diego, A. Abad, L.F. García, P. Gayan, J. Adanez, *Energy Fuel* 26 (2012) 791–800.
- [8] T. Ishigaki, S. Yamauchi, K. Kishio, J. Mizusaki, K. Fueki, *J. Solid State Chem.* 73 (1988) 179–187.
- [9] X.P. Dai, R.J. Li, C.C. Yu, Z.P. Hao, *J. Phys. Chem. B* 110 (2006) 22525–22531.
- [10] X.P. Dai, J. Li, J.T. Fan, W.S. Wei, J. Xu, *Ind. Eng. Chem. Res.* 51 (2012) 11072–11082.
- [11] O. Mihai, D. Chen, A. Holmen, *J. Catal.* 293 (2012) 175–185.
- [12] F. He, X.N. Li, K. Zhao, Z. Huang, G.Q. Wei, H.B. Li, *Fuel* 108 (2013) 465–473.
- [13] M. Ryden, A. Lyngfelt, T. Mattisson, D. Chen, A. Holmen, E. Bjorgum, *Int. J. Greenh. Gas Control* 2 (2008) 21–36.
- [14] Z. Sarshar, Z.K. Sun, D.Y. Zhao, S. Kaliaguine, *Energy Fuel* 26 (2012) 3091–3102.
- [15] A. Shafiefarhood, N. Galinsky, Y. Huang, Y.G. Chen, F.X. Li, *ChemCatChem* 6 (2014) 790–799.
- [16] L.M. Neal, A. Shafiefarhood, F.X. Li, *ACS Catal.* 4 (2014) 3560–3569.
- [17] L. Neal, A. Shafiefarhood, F.X. Li, *Appl. Energy* 157 (2015) 391–398.
- [18] C.T. Campbell, C.H.F. Peden, *Science* 309 (2005) 713–714.
- [19] K. Otsuka, Y. Wang, E. Sunada, I. Yamanaka, *J. Catal.* 175 (1998) 152–160.
- [20] Y.E. Zheng, Y.G. Wei, K.Z. Li, X. Zhu, H. Wang, Y.H. Wang, *Int. J. Hydrogen Energy* 39 (2014) 13361–13368.
- [21] K.Z. Li, H. Wang, Y.G. Wei, D.X. Yan, *J. Chem. Eng.* 156 (2010) 512–518.
- [22] K.Z. Li, H. Wang, Y.G. Wei, D.X. Yan, *Int. J. Hydrogen Energy* 36 (2011) 3471–3482.
- [23] A. Thursfield, A. Murugan, R. Franca, I.S. Metcalfe, *Energy Environ. Sci.* 5 (2012) 7421–7459.
- [24] K.S. Kang, C.H. Kim, K.K. Bae, W.C. Cho, S.H. Kim, C.S. Park, *Int. J. Hydrogen Energy* 35 (2010) 12246–12254.
- [25] H.H. Jeong, J.H. Kwak, G.Y. Han, K.J. Yoon, *Int. J. Hydrogen Energy* 36 (2011) 15221–15230.
- [26] D.D. Miller, R. Siriwardane, *Energy Fuel* 27 (2013) 4087–4096.
- [27] X. Zhu, K.Z. Li, Y.G. Wei, H. Wang, L.Y. Sun, *Energy Fuel* 28 (2014) 754–760.
- [28] K.S. Kang, C.H. Kim, K.K. Bae, W.C. Cho, W.J. Kim, Y.H. Kim, et al., *Int. J. Hydrogen Energy* 35 (2010) 568–576.
- [29] A. Sim, N.W. Cant, D.L. Trimm, *Int. J. Hydrogen Energy* 35 (2010) 8953–8961.
- [30] M. Alifanti, M. Florea, S. Somacescu, V.I. Parvulescu, *Appl. Catal. B* 60 (2005) 33–39.
- [31] R.D. Zhang, W. Yang, N. Luo, P.X. Li, Z.G. Lei, B.H. Chen, *Appl. Catal. B* 146 (2014) 94–104.
- [32] T.H. Shin, S. Ida, T. Ishihara, *J. Am. Chem. Soc.* 133 (2011) 19399–19407.
- [33] L.M. Liu, K.N. Sun, X.K. Li, M. Zhang, Y.B. Liu, N.Q. Zhang, X.L. Zhou, *Int. J. Hydrogen Energy* 37 (2012) 12574–12579.
- [34] G.Z. Zhang, Z. Zhao, J.F. Xu, J.X. Zheng, J. Liu, G.Y. Jiang, A.J. Duan, H. He, *Appl. Catal. B* 107 (2011) 302–315.
- [35] G.Z. Zhang, Z. Zhao, J. Liu, G.Y. Jiang, A.J. Duan, J.X. Zheng, S.L. Chen, R.X. Zhou, *Chem. Commun.* 46 (2010) 457–459.
- [36] N.D. Petkovich, S.G. Rudisill, L.J. Venstrom, D.B. Boman, J.H. Davidson, A. Stein, *J. Phys. Chem. C* 115 (2011) 21022–21033.
- [37] Y.C. Wei, J. Liu, Z. Zhao, Y.S. Chen, C.M. Xu, A.J. Duan, G.Y. Jiang, H. He, *Angew. Chem. Int. Ed.* 50 (2011) 2326–2329.
- [38] Y.C. Wei, J. Liu, Z. Zhao, A.J. Duan, G.Y. Jiang, C.M. Xu, J.S. Gao, H. He, X.P. Wang, *Energy Environ. Sci.* 4 (2011) 2959–2970.
- [39] Y. Liu, B.C. Liu, Q. Wang, C.Y. Li, W.T. Hu, Y.X. Liu, P. Jing, W.Z. Zhao, J. Zhang, *J. Catal.* 296 (2012) 65–76.
- [40] S.H. Xie, J.G. Deng, S.M. Zang, H.G. Yang, G.S. Guo, H. Arandiyan, H.X. Dai, *J. Catal.* 322 (2015) 38–48.
- [41] Y.X. Liu, H.X. Dai, J.G. Deng, X.W. Li, Y. Wang, H. Arandiyan, S.H. Xie, H.G. Yang, G.S. Guo, *J. Catal.* 305 (2013) 146–153.
- [42] K. Zhao, F. He, Z. Huang, A.Q. Zheng, H.B. Li, Z.L. Zhao, *Int. J. Hydrogen Energy* 39 (2014) 3243–3252.
- [43] P. Ciambelli, S. Cimino, L. Lisi, M. Faticanti, G. Minelli, I. Pettiti, P. Porta, *Appl. Catal. B* 33 (2001) 193–203.
- [44] R. Zhang, H. Alamdar, S. Kaliaguine, *J. Catal.* 242 (2006) 241–253.
- [45] K. Zhao, F. He, Z. Huang, G.Q. Wei, A.Q. Zheng, H.B. Li, Z.L. Zhao, *Appl. Energy* 168 (2016) 193–203.
- [46] X.Y. Wang, Q. Kang, D. Li, *Appl. Catal. B* 86 (2009) 166–175.
- [47] A.F. Carley, M.W. Roberts, A.K. Santra, *J. Phys. Chem. B* 101 (1997) 9978–9983.
- [48] J.L.G. Fierro, L.G. Tejeda, *Appl. Surf. Sci.* 27 (1987) 453–457.
- [49] S. Thirumalairajan, K. Girija, N.Y. Hebalkar, D. Mangalaraj, C. Viswanathan, N. Ponpandian, *RSC Adv.* 3 (2013) 7549–7561.
- [50] R. Si, Y.W. Zhang, S.J. Li, B.X. Lin, C.H. Yan, *J. Phys. Chem. B* 108 (2004) 12481–12488.
- [51] M. Kotobuki, R. Leppelt, D.A. Hansgen, D. Widmann, R.J. Behm, *J. Catal.* 264 (2009) 67–76.
- [52] D. Widmann, R.J. Behm, *Angew. Chem. Int. Ed.* 50 (2011) 10241–10245.
- [53] F. Mudu, B. Arstad, E. Bakken, H. Fjellvag, U. Olsbye, *J. Catal.* 275 (2010) 25–33.
- [54] J.G. Deng, H.X. Dai, H.Y. Jiang, L. Zhang, G.Z. Wang, H. He, C.T. Au, *Environ. Sci. Technol.* 44 (2010) 2618–2623.
- [55] F. Esch, S. Fabris, L. Zhou, T. Montini, C. Africh, P. Fornasiero, G. Comelli, R. Rosei, *Science* 309 (2005) 752–755.
- [56] O. Mihai, D. Chen, A. Holmen, *Ind. Eng. Chem. Res.* 50 (2011) 2613–2621.
- [57] A. Eyssler, A. Winkler, O. Safonova, M. Nachtegaal, S.K. Matam, P. Hug, A. Weidenkaff, D. Ferri, *Chem. Mater.* 24 (2012) 1864–1875.
- [58] Y.H. Chin, C. Buda, M. Neurock, E. Iglesia, *J. Am. Chem. Soc.* 133 (2011) 15958–15978.
- [59] A. Kubacka, R. Si, P. Michorczyk, A.M. Arias, W.Q. Xu, J.C. Hanson, J.A. Rodriguez, *Appl. Catal. B* 132–133 (2013) 423–432.
- [60] R.C. Stehle, M.M. Bobek, R. Hooper, D.W. Hahn, *Int. J. Hydrogen Energy* 36 (2011) 15125–15135.